Synthesis and Property Characterization of the MXenes

by

Mofetoluwa Fagade

A Thesis Presented in Partial Fulfillment
of the Requirements for the Degree
Master of Science

Approved February 2023 by the
Graduate Supervisory Committee:

Kenan Song, Chair
Beomjin Kwon
Qiong Nian

ARIZONA STATE UNIVERSITY

May 2023

ABSTRACT

Nanomaterials redefine the lens through which the world is viewed today. The miniaturization of devices and systems to the nanoscale explodes the realm of what is possible as the interactions with neighboring atoms and molecules increase. This interactivity creates ripple effects that lead to superior mechanical, thermal, electrical, and optical properties that are highly desired across several industries. Two-dimensional (2D) materials are a branch of this family, and the focus of this paper revolves around a recent addition to this category called MXenes. The versatile properties of these 2D nanomaterials have made them unique, as they have the desired performance that can be utilized in several industries, especially energy management, wastewater treatment, and microelectronic devices. Followed by the MAX phase synthesis, hydrofluoric (HF) acid has been the primary etchant utilized to derive these 2D nanoparticles. However, alternative etchants via reactions are desirable to achieve similar selective etching without involving highly toxic HF. Therefore, this study investigated MXene synthesis and applications in 3D printing, followed by the formation of the precursor MAX, an optimized in-situ etching method, and streamlined post-etching processes to maximize 2D MXene yield. The etched powders were then analyzed using scanning electron microscopy (SEM), x-ray diffraction (XRD), atomic force microscopy (AFM), and energy-dispersive x-ray spectroscopy (EDS) characterization methods to verify and validate the MXene dimensions, chemistry, and crystal structures. Simple applications, such as the dispersion feasibility for customizing micropatterns via 3D printing, were also demonstrated as examples. Finally, this research showed the simple processing of 2D MXenes and their potential in structural support, heat dissipation, microelectronics, optical meta-surfaces, and other areas.

ACKNOWLEDGMENTS

I would like first to thank my advisor, Dr. Song, for letting me join his lab and allowing me access to state-of-the-art equipment and materials to carry out this project effectively. I appreciate all the time he has given me over the past year, and I am thankful for his guidance and counseling.

I would also like to thank the committee members, Dr. Qiong Nian and Dr. Beomjin Kwon, for taking time for my thesis and defense. In addition, I would also like to give my special thanks to my lab mates, Dhanush Patil, Sayli Jambhulkar, Mohammed Bawareth, Dharneedar Ravichandran, Yuxiang Zhu, and Nathan Fonesca, for their help and support throughout the project. This thesis was completed with the exceptional assistance of Dhanush Patil and Sayli Jambhulkar. They guided me while I got up to speed on the subject matter and helped me perform characterizations after the material synthesis. I am grateful to them for sparing time out of their projects to help me complete this thesis.

Finally, I would like to give a special shoutout to my family. They stood with me through thick and thin and allowed me to persevere, especially when things were rough. Their constant advice and encouragement played a significant role in why I can submit my complete thesis today.

TABLE OF CONTENTS

Page

LIST OF TABLES v

LIST OF FIGURES vi

LIST OF ABBREVIATIONS viii

CHAPTER

1 INTRODUCTION 1

Overview 1

Background and Literature Review 5

MAX Phase 5

MXenes 8

2 MAX AND MXENE SYNTHESIS 17

Materials 17

MAX Phase Synthesis 18

MXene Synthesis 18

Characterizations 19

Results and Discussions 20

3 DEMONSTRATIONS OF MXENE APPLICATIONS 23

Materials 23

Characterizations 23

Results and Discussions 24

4 CONCLUSIONS 28

REFERENCES 29

LIST OF TABLES

Table Page

1. Classifications and Features of Nanomaterials[1] 3

2. Summary of MXenes and Their Synthesis Protocols 14

LIST OF FIGURES

Figure Page

1. Schematic Illustration Showcasing Most Common Members of the Two-Dimensional (2D) Materials Family as Follows a) MXenes[2], b) Layered Double Hydroxides (LDHs)[3], c) Graphene, d) Transition Metal Dichalcogenides (TMDCs), e) Metal-Organic Frameworks (MOFs), f) Hexagonal Boron Nitride (h-BN)[4], g) Covalent-Organic Frameworks (COFs)[5], h) Silicate Clays[6], i) Black Phosphorus[7], j) Oxides.[8] .....……..……...…4

2. Elemental Constituents of the MAX Phase with Basic Symbols Used to Distinguish Between Different Components.[9] ……...…...4

3. Elemental Constituents Are Currently Employed in Literature to Form MXenes. This Group Is More Selective than Those Used in the MAX Phase ….....8

4. Process Flowchart Illustrating the Experimental Steps Involved in the Synthesis of MXenes From Elemental Powders of MAX Phase to Colloidal $Ti_3C_2T_x$-ink Solutions.…..……..….17

5. Characterizations of MAX Phase and MXene Throughout the Synthesis Process. a.) Frontal SEM Micrograph of MAX Phase Showcasing Uniform Surface Morphology and Kink Bands, b – c.) Cross-sectional SEM Imaging of Ti_3AlC_2 at Different Resolutions and Magnifications, d.) Cross-sectional SEM Imaging of Multi-layered $Ti_3C_2T_x$ Illustrating Capacious Spacing Between Layers After Etching, e – f.) Delaminated $Ti_3C_2T_x$ Sheets at Different Resolutions, g_1 – g_2.) AFM Images Depicting Cross-sectional Thickness of a Multi-layered $Ti_3C_2T_x$ Stack along the Horizontal Plane, h.) WAXD Diffraction Patterns of Ti_3AlC_2

Figure Page

Before and After Etching Displaying Intensities of MAX Phase and Resulting MXene Respective Phase Angles. ……..……..…..…..22

6. a – c.) Viscoelastic Properties of 30, 50, 100, and 200 mg mL^{-1} Aqueous $Ti_3C_2T_x$ Ink Solutions, d – e.) Printed Rectilinear and Zig-zag patterns of 100 mg mL^{-1} $Ti_3C_2T_x$Ink, f.) Conductivity vs Concentration Chart for Aqueous Ink Solutions, g_1 – g_2.) CV Graph Highlighting Electrochemical Properties of $Ti_3C_2T_x$ – coated Electrode at Multiple Scan Speeds. ……...……..…27

LIST OF ABBREVIATIONS

0D	Zero-dimensional
1D	One-dimensional
2D	Two-dimensional
AFM	Atomic force microscopy
Al	Aluminum
BN	Boron nitride
BP	Black phosphorus
COF	Covalent-organic framework
DI	Deionized
DMA	Dynamic mechanical analysis
DSC	Differential scanning calorimetry
EDS	Energy-dispersive X-ray spectroscopy
GO	Graphene oxide
HIP	Hot-isostatic pressing
HP	Hot pressing
LDH	Layered doubled hydroxide
MOF	Metal-organic framework
PDS	Pulse discharge sintering
PS	Pressureless synthesis
RPM	Revolutions per minute
SEM	Scanning electron microscope
SHS	Self-sustaining high-temperature synthesis

SPS	Spark plasma sintering
TGA	Thermogravimetric analysis
Ti	Titanium
TiC	Titanium carbide
TMDC	Transition metal dichalcogenide
TMO	Transition metal oxide
WAXD	Wide-angle X-ray diffraction

CHAPTER 1

INTRODUCTION

1.1 *Overview*

Since the mechanical cleavage from graphite in 2004, graphene has shown the considerable potential of revolutionizing the semiconductor industry,[1] which also attracted massive interest in studying graphene and similar two-dimensional (2D) nanomaterials.[10,113] The superior properties displayed by 2D nanoparticle families are closely relevant to their dimensions (e.g., smaller than 100 nm), chemistry (e.g., elements and compositions), and crystallization features (e.g., HCP with close packing or gyroids with porosity).[11–39] For example, the defects will be minimized when the particle size reached the nanoscale, which is essential for nanoparticles to display high intrinsic physical and chemical properties.[13,15,19,21–23,26,31–33,36] Graphite, a natural-occurring crystalline allotropic form of carbon, is known for its lubrication effects. However, the weak van der Waals forces between the layers lead to mechanical weakness. Graphene, its carbon counterpart with atomic layer thickness, shows mechanical strength, good electrical conductivity, and high optical permeability, among many others.[11,23,28,30]

Classification of nanomaterials is based on several properties (**Table 1**), such as dimensionality, chemical composition, morphology, and crystallization behavior.[31–33,37] In this thesis, the focused categorization based on dimensionality will be 2D layered nanoparticles, namely, MXenes. Overall, this study aims to summarize the MXene synthesis methods, pinpoint obstacles commonly faced in the current state of the art and streamline the process by demonstrating the synthesis of titanium carbide-based MXene as an example. Last but not the least, the patterning capability via 3D printing also showed

potential applications in cellular solids, heat dissipation, printed circuit board, and coating optics.

Although the 2D material family is rapidly expanding (**Figure 1**), several members have not yet found industrial applications due to a few technical challenges. For example, there is a limit to the scalability of high-quality graphene layers, such as the high defect density in mechanically-exfoliated graphene or the high cost associated with vapor deposition methods.[1] Besides, single-layer graphene nanomaterials are thermodynamically unstable, and their noncontinuous powder state needs high-resolution nanomanufacturing to prevent oxidation and form high precision.[1] On the other hand, a few contenders have emerged and could rival graphene due to their potential applications and versatility across several industries.[1] MXenes, the subject of this paper, composed of 2D carbides, nitrides, and carbonitrides, are firmly entrenched in the second category. MXenes are a family of two-dimensional (2D) transition metal carbides, nitrides, and carbonitrides with the general formula $M_{n+1}X_nT_x$ (n=1,2,3) where M represents the transition metal (usually Ti, Ta, Nb, V, Mo), X can either be C or N and T represents the surface termination groups (-OH,-F,-O).[1,9,40–66]

Table 1. Classifications and features of nanomaterials[1]

Number of Nanoscopic Dimensions	**Specific surface area (area per unit volume with r, the radius of the sphere or the cross-section; l, length; w, width; t, thickness)**	**Categories**	**Advantages**	**Typical challenges**	**Examples**	**Ref.**
0D with an aspect ratio of 1	*SSA = 3/ (R * p)* *where SSA = specific surface area, R=avg. particle size, and p = density of the material.*	Nanospheres	Simple assembly features due to uniform dimensions along x/y/z axes	Size control during powder-generation	fullerene, metal nanoballs, inorganic quantum dots, and magnetic and noble metal nanoparticles.	[21,31–37,67]
1D with an aspect ratio [1, 10^9]		Nanotubes, nanowires, nanowhiskers	Large aspect ratios that can efficiently transfer stress and direct electron/phonon transport	Continuity of in-situ growth or long-range order management for non-continuous powders	Carbon nanotubes, silver nanowires, gold nanowhiskers, carbon nanofibers, zinc oxide nanorods, and polymer nanofilaments	
2D with an aspect ratio of [1, ∞]		Nanosheets, nanoplatelets, nanolayers	Unique electronic and superconducting performance	Synthesis of individual layers and their 2D structural retaining during processing	Graphene, MXene, black phosphorus	

Note: 0D, zero-dimensional; 1D, one-dimensional; 2D, two-dimensional

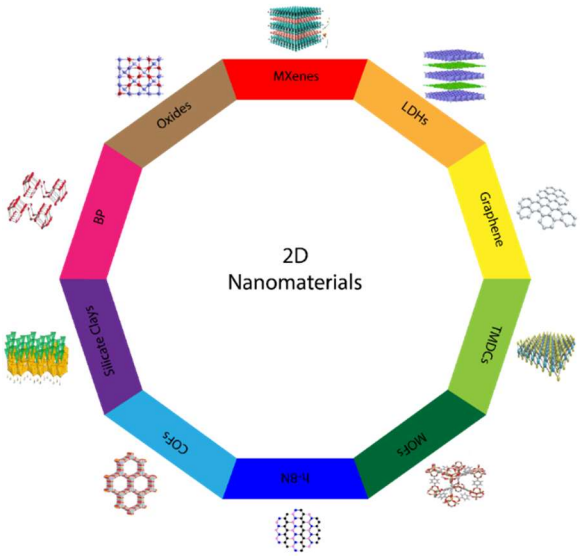

Figure 1. Schematic illustration showcasing most common members of the two-dimensional (2D) materials family as follows: a) MXenes[2], b) layered double hydroxides (LDHs)[3], c) graphene, d) transition metal dichalcogenides (TMDCs), e) metal-organic frameworks (MOFs), f) hexagonal boron nitride (h-BN)[4], g) covalent-organic frameworks (COFs)[5], h) silicate clays[6], i) black phosphorus[7], j) oxides.[8]

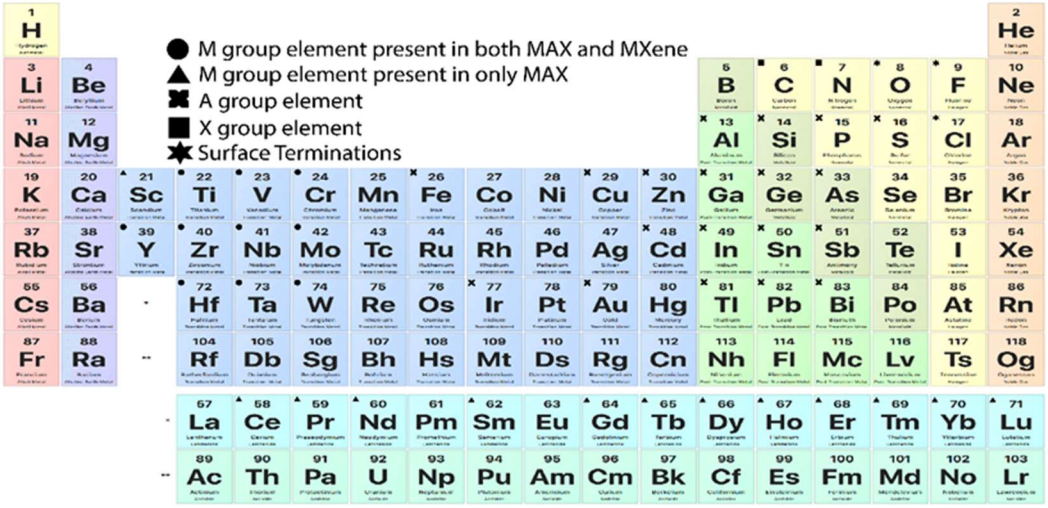

Figure 2. Elemental constituents of the MAX phase with basic symbols used to distinguish between different components.[9]

Furthermore, a few properties have set MXenes apart from other family members and are highlighted below. First, various compositions and structures can be formed in MXenes, leading to a rapidly growing group.[1,43] For example, the MXene family has seen a group of carbines, nitrides, and carbonitrides (e.g., Ti, V, Cr, Y, Zr, Nb, Mo, Hf, Ta, W-based, **Figure 2**). Second, the space between the MXene sheets is also highly versatile and amenable to a host of compounds and cations (e.g., Li, Na, K, Rb, Cs, Mag, Ca, Sr, Ba, and others, **Figure 2**). This allows the layered MXene to be intercalated with various organic molecules and used as exfoliated layer reinforcements in matrix materials (e.g., polymers).[9] Last but not least, synthesized MXenes also display unique properties of being simultaneously electronically conductive and hydrophilic (e.g., -H, -OH, -F, -Cl, **Figure 2**).[9]

As the syndication of MXenes is a relatively recent discovery and addition to the field of two-dimensional materials, this thesis will focus on MXene synthesis with a demonstration of titanium carbide-based MXene (i.e., Ti_3AlC_2). Specifically, this thesis first summarizes the background and current state of the art in the MAX and MXene synthesis (**Chapter 1**). Second, the synthesis of MAX and MXene will be detailed with characterization results and discussions (**Chapter 2**), followed by their application as surface patterns enabled in 3D printing methods (**Chapter 3**). Finally, the thesis will be concluded with an overview of challenges that need to be overcome in future work (**Chapter 4**).

1.2 *Background and Literature Review*

1.2.1 *MAX Phase*

As can be seen in **Figure 3**, the different elements of a MAX phase are usually as follows:[1]

a) M represents an early transition metal (e.g., Ti, V, Cr, Y, Zr, Nb, Mo, Hf, Ta, W)
b) A is typically a group IIIA or IVA element (e.g., Al, Si, Ge, Sn, S, As, P, In, Ga, Ti, Pb)
c) X is the termination element (e.g., -O, -F, -OH groups)

Due to the two distinct layers, the MAX phase usually contains a covalent, ionic, or metallic bond in the M-X layers while the M-A bond is weakly bonded.[68] MAX phases began garnering interest more than twenty years ago when they were spotlighted by Dr. Barsoum.[69] The family which is comprised of nano-layered ternary carbides and nitrides drew attention due to their unique combination of properties.[70] These included damage tolerance, low hardness, high strength, structural stability at high temperatures (> 1200 ^{o}C), high electrical and thermal conductivity, and machinability comparable to graphite.[70] Members of this family usually have a structural format of $M_{n+1}AX_n$ where n determines the phase of the material[71]. M_2AX, M_3AX_2, and M_4AX_3 are the most common iterations and are referred to as the 211,312, and 413 phases. Larger values of n such as 514 and 615 have been reported occasionally.[71] MAX phases are usually synthesized by hot isostatic pressing (HIP), hot pressing (HP), spark plasma sintering (SPS), mechanical alloying (MA), or through self-propagating high-temperature synthesis. [71,72]

HP and HIP were the methods initially utilized to produce MAX phases.[73] The hot pressing method is designed to form a dense compact material which it achieves by creating a high-pressure, high-temperature, and low strain-rate environment.[73] Hot isostatic

pressing method is similar with regards to its simultaneous application of high temperature and pressure with the slight change in the type of pressure from uniaxial to isostatic. As a result, the pressure is induced uniformly in all directions with this method.[73] To counteract the formation of impurities and attempt the synthesis of monophasic MAX material, Hong et al. utilized spark plasma sintering. The exact nature of the SPS mechanism is still unclear as there have been a few hypotheses.[74] It was theorized at first that SPS had a thermal diffusion regime that was active for lower temperatures and a volume diffusion method for higher temperatures.[75] It was then described as a self-adjusting mechanism which was then followed by a sequencing theory.[76,77]

Regardless of its underlying mechanism, SPS eliminates the gaps and forms metallurgical bonds between particles which are the two prerequisites to forming high-density bulk materials.[74] This method is particularly attractive because the densification of powders can be achieved in relatively milder conditions compared to HP and HIP methods.[78] In addition, it can be used to consolidate powders that have been synthesized using the self-propagating high-temperature synthesis (SHS) method.[79] The SHS method involves highly exothermic reactions which once ignited self-propagate throughout the mixture in the form of a combustion wave.[78] This process is also particularly attractive because no other secondary phases are usually found in the final product. This is a consequence of the self-cleaning nature of this process as impurities are purged away due to the high temperature of combustion. [79,80]

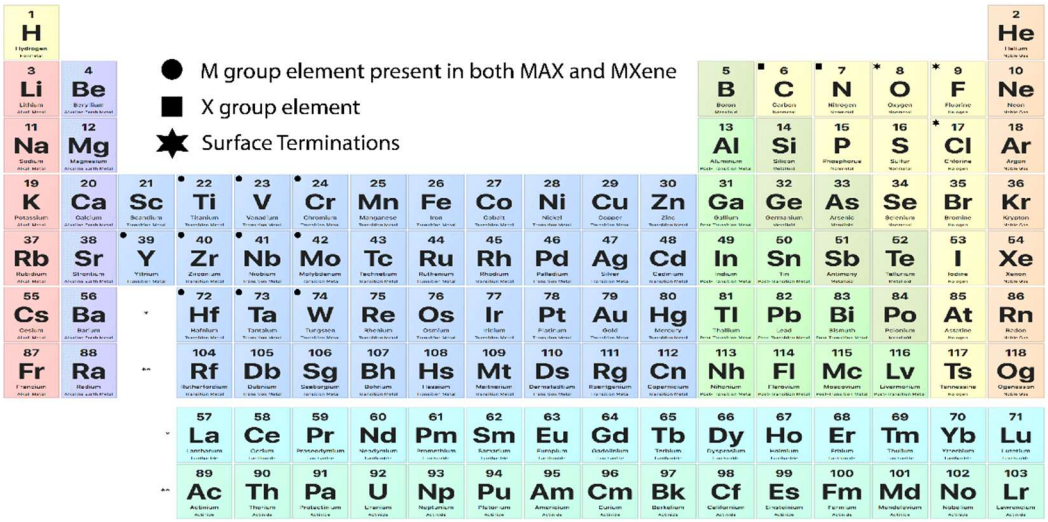

Figure 3. Elemental constituents are currently employed in literature to form MXenes. This group is more selective than those used in the MAX phase.

Ti_2AlC and Ti_3AlC_2 are the most lightweight and oxidation-resistant layered ternary carbides in the MAX phases, which is why they are some of the commonly used precursors.[71] All the above-mentioned methods have been used to process Ti_3AlC_2, and for this project, SHS would be the focus due to its operational simplicity. Besides, the SHS takes advantage of the heat from the exothermic reactions between the powders, thus requiring less time and relatively less energy.[71]

1.2.2 *MXenes*

Two approaches in general can be used to obtain 2D materials, including MXene. The first strategy is the bottom-up approach that involves deposition methods to synthesize the 2D layers. For example, chemical vapor deposition (CVD) starts from atomic carbon deposition. Still, the main challenges include the precise control of single layers, strict requirements of high pressure and gas flow, slow reaction, and high cost.[81] The second

approach is a top-down approach and is more commonly used due to its cost-efficiency and manufacturing processability. This method involves the exfoliation of the 3D layer counterparts.[81] Specifically, mechanical and chemical exfoliations are two techniques used in the literature for this approach. An example of mechanical exfoliation can be seen using adhesive tape to peel graphene from graphite due to the weak van der Waals force between the layers.[81] However, this is unsuitable for the MAX precursors due to the strong covalent and metallic bonds between the M elements and Al.[81] Chemical exfoliation is the route that is commonly employed when strong bonds between the layers are involved, e.g., when deriving MXenes from their MAX precursor phases.[1,9,43,45,71,81,82] It is also important to note that before MXene synthesis, it was thought that only weakly bonded three-dimensional solids could be exfoliated.[81] Thus, this research was groundbreaking in the field. During the chemical exfoliation process, the A-element layers must be etched explicitly from $M_{n+1}AX_{n,}$ thus resulting in metal carbides and nitrides with the general chemical formula $M_{n+1}X_n$. As a result of this etching, the functional groups are usually denoted as $T_{x,}$ which results in $M_{n+1}X_nT_{x.}$ A few etching techniques have been employed in the literature and will be briefly reviewed in **Table 2** and discussed below.

1) HF Etching

HF etching is a top-down approach usually classified under wet etching. The etching process takes advantage of the reaction and elimination of A layers from the precursor MAX phases. Due to the chemical activeness of the weakly bonded layers, selective etching is possible. Simultaneously, the remaining MX layers are terminated with the

surface groups mentioned above. Using one of the more popular titanium carbide precursors ($Ti_3C_2T_x$) as a reference, the possible reactions occur as shown below.[40,83]

$$Ti_3AlC_{2\,(s)} + 3HF_{\,(aq)} = Ti_3C_{2\,(s)} + AlF_{3\,(aq)} + 1.5H_{2\,(g)} \quad (1)$$

$$Ti_3C_{2\,(s)} + 2HF_{\,(aq)} = Ti_3C_2F_{2\,(s)} + H_{2\,(g)} \quad (2)$$

$$Ti_3C_{2\,(s)} + 2H_2O_{\,(aq)} = Ti_3C_2(OH)_{2\,(s)} + H_{2\,(g)} \quad (3)$$

$$Ti_3C_2(OH)_{2\,(s)} = Ti_3C_2O_{2\,(s)} + H_{2\,(g)} \quad (4)$$

The HF concentration, etching temperature, and etching time are critical parameters that affect the morphology and characteristics of the resulting MXenes.[81,83] For example, 50 wt.% HF was initially used. Though effective, lower concentrations were optimized due to less HF toxicity (e.g., 5 wt.%). Due to the toxic and corrosive risks involved with the HF etchant, other methods have been developed to prevent direct interaction/contact with HF.[83] For example, In Situ HF-Forming Etching Methods usually comprises two species interacting in spontaneous and self-terminating reactions that create the essential HF. This helps prevent direct contact with the etchant.[83] The following processes fall under that umbrella and are briefly highlighted.

2) Acid/Fluoride Salt Etching

This is the most common two-reactant combination in literature today, which was first reported by Ghidiu[84] in 2014 and involved the etching of TI_3AlC_2 at 40 °C using an HCL/LiF solution.[83] Conductive $Ti_3C_2T_x$ clay was produced using this method, and some of its properties included high plasticity and the ability to be made into a film using Roll-to-Roll pressing.[83] Like the HF etching, the HCl/LiF etching process also creates multi-layered MXenes. The process was then further refined, and as it matured, more

configurations of fluorides and acids could be used. Furthermore, the interlayer spacing of the MXenes was directly regulated by the fluoride salts that can alter the layer parameter based on desired properties.[9] The minimally intensive layer delamination (MILD) method has been preferred among current approaches based on salt etching because single and larger flakes are produced with fewer defects.[45]

3) Bifluoride Salts Etching

This method was first reported during the etching of epitaxial Ti_3AlC_2 films at room temperature with the application of NH_4HF_2[85]. In this process, the hydrated cations from the bifluoride salts are dissociated and adsorbed on the negatively charged surface of the MXenes. This leads to an enlargement of the interlayer spacing, as shown in the following equations.[85]

$$Ti_3AlC_2 + 3NH_4HF_2 = (NH_4)_3\ AlF_6 + Ti_3C_2 + 1.5H_2 \quad (5)$$

$$Ti_3C_2 + aNH_4HF_2 + bH_2O = (NH_3)_c\ (NH_4)_d\ Ti_3C_2\ (OH)_x\ F_y \quad (6)$$

Since its initial procedures in 2014, the range of bifluoride salt etching has increased from thin epitaxial films to powders. This synthesis process is beneficial when creating MXenes for water-sensitive applications and is preferred due to HF due to its higher operating safety.[83] TI_3AlC_2 is the only precursor etched using this method, with more work being explored to determine the suitability to etch other MAX phases.[83] The direct and in-situ HF methods are typically performed at temperatures less than 60 ^oC, but MXenes can also be obtained at higher temperatures. For example, blending NH_4F with the low eutectic solvent mixed with chlorine chloride and oxalic acid can etch the MAX phase using a hydrothermal process, generating temperatures ranging from 100-180^oC.[86]

4) Alkali Etching Methods

The above methods utilize acids as etchants, but low-concentration alkalis can also be used to etch the MAX phase selectively. The main drawback of this method is that only the superficial layer of the precursor is etched, resulting in a meager MXene yield.[83] This obstacle can be circumvented if the alkali concentration and temperature increase to a certain threshold. For example, Al was selectively etched from TI_3AlC_2 using 27.5 M NaOH, resulting in 92 wt.% MXene yield.[87] During this process, Al follows common pathways by transforming into Al (oxide) hydroxides before dissolution in the alkaline etchant (see reactions below).[83]

$$Ti_3ALC_2 + OH^- + 5H_2O = Ti_3C_2(OH)_2 + Al(OH)_4^- + 2.5H \quad (7)$$

$$Ti_3AlC_2 + OH^- + 5H_2O = Ti_3C_2O_2 + Al(OH)_4^- + 3.5H_2 \quad (8)$$

In addition, using concentrated alkali for etching the MAX phase efficiently produces hydrophilic products with F-free terminations.[83] However, increasing the scalability of MXene utilizing this method is extremely difficult due to the dangers associated with high-temperature concentrated alkali solutions.[83]

5) Electrochemical Etching Methods

The preparation of MXenes using this route involves the selective etching away of the Al layer under a specific voltage using its MAX precursor as an electrode.[83] The typical voltage used during this technique varies between 0 and 2.5 V, which results in the break in the M-A bond, thus allowing for the successful removal of selective layers.

Consequently, the modulation of the etching voltage and etching time are the main parameters that allow for accurate control and fine-tuning of the etching process[83].

Although it has several advantages, the main drawback is a result of the low yield. Plus, this method develops the carbide-derived carbon (CDC) layer, which forms due to the etching process and prevents subsequent etching processes.[83] The etching reactions are described below.[83]

$$Ti_3AlC_2 - 3e^- + 3\ Cl^- = Ti_3C_2 + AlCl_3 \quad (9)$$

$$Ti_3C_2 + 2OH^- - 2e^- = Ti_3C_2(OH)_2 \quad (10)$$

$$Ti_3C_2 + 2H_2O = Ti_3C_2(OH)_2 + H_2 \quad (11)$$

The following processes all classify as molten salt etching methods, which have been explored due to their increased versatility as opposed to the other etching routes, which only etch Al-containing MAX phases. Furthermore, the whole process is exponentially faster than different routes, as the entire manufacturing process can be completed in a matter of hours rather than days[88].

6) Fluoride-Containing Molten Salt Etching Method

As referenced earlier, other etching routes fail to produce MXenes when using non-Al or nitrides MAX phases. As a result, this method is the first choice for synthesizing MXenes with high formation energy.[83] The main drawback is the developed terminations, which is why fluorine-free molten salt methods are required.[83]

7) Fluoride-free Molten Salt Etching Method

In this molten salt etching method, a $ZnCl_2$/NaCl/KCl molten salt system is under a nitrogen-protected environment.[83] In this system, $ZnCl_2$ was used as the etchant, while stoichiometric quantities of NaCl and KCl in the molar ratio of 1:1 formed the salt bath and reduced the melting point of the eutectic system. The etching process is described in

the equations below.[83] As the process is fluoride-free and nonaqueous, the MXene is full of -Cl terminations instead of -F, -O, and -OH.[83]

$Ti_3AlC_2 + 1.5ZnCl_2 = Ti_3ZnC_2 + 0.5Zn + AlCl_3$ (12)

$Ti_3ZnC_2 + ZnCl_2 = Ti_3C_2Cl_2 + 2Zn$ (13)

8) Other etching processes

These processes include using an alkali-assisted hydrothermal method, which synthesized $Ti_3C_2T_x$ at 270 ºC. In addition to this, the first nitride MXene produced, $Ti_4N_3T_x$, was created using a molten salt eutectic mixture of lithium fluoride (LiF), sodium fluoride (NaF), and potassium fluoride (KF) at 550 ºC under the flow of argon.[81]

Table 2. Summary of MXenes and their synthesis protocols

Methods	MXenes	Precursors	Etchants	Etching Conditions	Surface Termination Groups	Ref.
Direct HF etching methods	$Ti_3C_2T_x$	Ti_3AlC_2	50 wt% HF	RT, 2 h	-OH,-O,-F	57
	V_2CT_x	V_2AlC	50 wt% HF	RT, 90 h		89
	Nb_2CT_x	Nb_2AlC	50 wt% HF	RT, 90 h 55 ºC, 40 h		
	$Nb_4C_3T_x$	Nb_4AlC_3	50 wt% HF	RT, 96 h		90
	$Ta_4C_3T_x$	Ta_4AlC_3	50 wt% HF	RT, 72 h		66
	Ti_3CNT_x	Ti_3AlCN	50 wt% HF	RT, 18 h		
	Mo_2C	$Mo_2Ga_2C_2T_x$	50 wt% HF	55 ºC, 160 h		65
	$Hf_3C_2T_x$	$Hf_3(AlSi)_4C_6$	50 wt% HF	RT, 60 h		64
	$Zr_3C_2T_x$	$Zr_3Al_3C_5$	50 wt% HF	RT, 72 h		91
	Mo_4VC_4	Mo_4VAlC_4	50 wt% HF	50 ºC, 192 h		63
	$Ti_3C_2T_x$	Ti_3SiC_2	30 wt% HF/35 wt% H_2O_2	40 ºC, 45 h 40 ºC, 45 h		50

			30 wt% HF/10 ml 1.85 M $(NH_4)_2S_2O_8$			
			40 ml 30 wt% HF/10 ml 2.5 M KO_4	40 ºC, 45 h		
			40 ml 30 wt% HF/10 ml 1.25 M $FeCl_3$	40 ºC, 45 h		
			37.5 ml 20 wt% HF/2.5 ml HNO_3	RT, 40 h		
In situ HF formation etching	Ti_2CT_x	Ti_2AlC	6 M LiF + 0.9 M HCl	40 ºC, 15 h	-O,-OH,-F	85
			4 M NaF + 12 M HCl	60 ºC, 24 h		86
			4 M KF + 12 M HCl	40 ºC, 48 h		
			4 M NH_4F + 12 M HCl	40 ºC, 48 h		
			2 g FeF_3 + 6 M HCl	60 ºC, 25 h		43
	$Ti_3C_2T_x$	Ti_3AlC_2	1 M $NaHF_2$	60 ºC, 24 h		36
			1 M KHF_2	60 ºC, 24 h		
			2 M NH_4HF_2	RT, 24 h		39
			12 M LiF + 9 M HCl	RT, 24 h		
			2 g FeF_3 + 6 M HCl	60 ºC, 50 h		43
			4 M NaF + 12 M HCl	40 ºC, 48 h		34
			4 M NH_4F + 12 M HCl	40 ºC, 48 h		

Alkali Etching	$Ti_3C_2T_x$	Ti_3AlC_2	1 M NaOH + 1 M H_2SO_4	80 °C, 100 h + 80 °C, 2 h	-OH,-O	[87]
	$Ti_3C_2T_x$	Ti_3AlC_2	27.5 M NaOH	270 °C, 12 h		[88]
			1.25 M KOH	180 °C, 24 h		[42]
Electrochemical Etching	$Ti_3C_2T_x$	Ti_3AlC_2	1 M NaOH + 0.2 M TMAOH	5 V, 5 h	-OH,-O,-Cl	[89]
	Ti_2CT_x	Ti_2AlC	2 M HCl	0.6 V, 120 h		[90]
			1 M HCl	0.3 V, 9 h, 50 °C		
Molten Salt Etching	Ti_2CT_x	Ti_2AlC	$ZnCl_2$	550 °C, 5 h, Ar	-O,-Cl	[91]
			$CuCl_2$	650 °C, 24 h, Ar		[92]
			$CdCl_2$	650 °C, 24 h, Ar		
	$Ti_3C_2T_x$	Ti_3AlC_2	$FeCl_2$	700 °C, 24 h, Ar		
			$CoCl_2$	650 °C, 24 h, Ar		
			$NiCl_2$	650 °C, 24 h, Ar		
			I_2	100 °C	-O,-OH,-F	[50]
Other etching methods	Mo_2C	Mo_2Ga_2C	Ultraviolet light(100W)	3-5 h	-O	[93]
	$Ti_3C_2T_x$	Ti_3AlC_2	Surface Acoustic waves (SAWs), LiF(≈ 0.05 M)	Millisecond	-O,-OH,-F	[94]
	Ti_2CT_x	Ti_2SC	Thermal reduction strategy	400-900 °C, 30 min, Ar/H_2	-O,-OH	[95]
	$Ti_2C_2T_x$	Ti_2AlC_2	Algae	RT, 1 day		[96]

CHAPTER 2

MAX AND MXENE SYNTHESIS

2.1 *Materials*

Titanium carbide (TiC) (i.e., avg. particle size ~2 mm, 99.5 % purity), aluminum (Al) (i.e., avg. particle size ~325 mesh, 99.5 % purity), and titanium (Ti) (i.e., avg. particle size ~325 mesh, 99.5 % purity) powders were obtained from Alfa Aesar. All materials were purchased and used without further treatment. **Figure 4** shows the flow chart describing the synthesis of MAX and MXene phases, with details explained below.

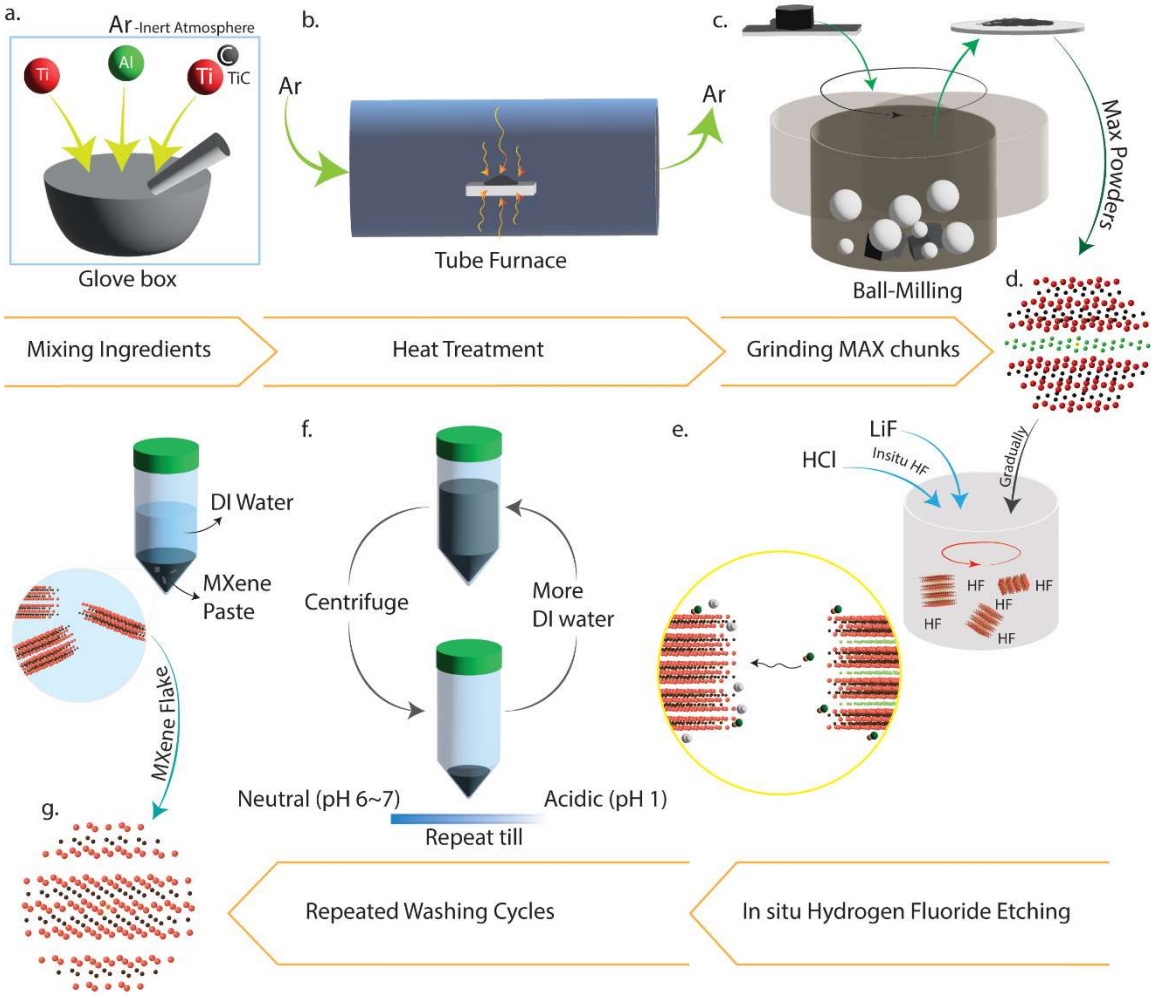

Figure 4. Process flowchart illustrating the experimental steps involved in the synthesis of MXenes from elemental powders of MAX phase to colloidal $Ti_3C_2T_x$ ink solutions.[92]

2.2 *MAX Phase Synthesis*

MAX powders were synthesized by mixing TiC, Al, and Ti powders in the molar ratio 2:1.1:1.[54] The mixing was carried out under an argon-purged environment in a glovebox (VTI Universal, Gloucester, MA, U.S.). This inert atmosphere was used to prevent oxidation during the mixing and grinding. The homogeneous mixture was then transferred to the tube furnace and heated under uniform argon flow in an alumina crucible (**Figure 4b**). It comprised three stages, including the (i) ramp-up stage, where the powders were heated from room temperature to 1350 ºC at a constant rate of 5 ºC/min, (ii) soaking stage, where a maximum temperature of 1350 ºC was held for 2 h, and (iii) cooling stage from 1350 ºC to the room temperature. As a result of the sintering, the loosely packed powders agglomerated as hard, chalky flakes that were then ground into fine powders using a planetary ball mill **(**F-P2000 Focucy High-energy, Changsha, HN, China) (**Figure 4c).** During the milling process, multiple runs of rates greater than 200 rpm were performed for at least 15 min per cycle to ensure that the flakes were reduced to a small-enough size before sieving.

The milled powders were then passed through a 400-mesh sieve to obtain uniformly distributed powders of ~38 μm for the particle size.[54] As a result of these procedures, ~0.2 g of the powder was lost between heat treatment and milling, resulting in a 94 % yield for each run.[54]

2.3 *MXene Synthesis*

During the etchant preparation, 74.7 ml of 12 M HCl was diluted with 100 ml of DI water to form a 9 M HCl solution. Subsequently, LiF powder (0.8 g) was gradually dissolved in 10 ml of 9 M HCl solution under constant magnetic stirring with a rate of 500 rpm for 10 min to form desirable concentrations. Once the acidic solution had entirely dissolved the LiF salt, 0.5 g of MAX phase powder was gradually added to the etchant solution (i.e., HCl/LiF). This addition was done slowly to avoid severe reactions experienced during abrupt MAX addition in etchants.[45,54] This mixture was then magnetically stirred at 500 rpm for 24 h at 35 ºC.

After the delamination procedure, the exfoliated mixture was collected and washed several times to neutralize the acidic pH of the mix. First, DI water was added to the mixture and placed in the centrifuge for washing. Each cycle was performed at 3500 rpm for 10 min. This step was repeated till the pH of the supernatant was ~ 6. The slurry suspensions were then collected and dispersed in deaerated water. This colloid was then delaminated using sonication via the bath and tip sonicators for 30 min each, with the latter being completed under flowing argon to avoid oxidation. Followed with the centrifugation at a rate of 3500 rpm for 1 h, the stable colloidal supernatant was collected, and vacuum filtered through a PVDF membrane. A thin film was formed on the filtration membrane (**Figure 4**). The flakes were then dispersed in different solvents (e.g., 50 mg mL^{-1} aqueous DI water, 50 mg mL^{-1} ethanol, 50 mg mL^{-1} methanol) and stored at low temperatures to prevent degradation (**Figure 4**).

2.4 Characterizations

Morphological studies of the heat-treated MAX and MXene powders were performed using a Zeiss Auriga high-resolution field emission scanning electron microscopy (SEM). This SEM was coupled with an Everhart-Thornley (E-T) detector to capture EDS images. The resolution was manually operated and optimized to produce high-quality images. The surface structure and characteristics of MAX and MXene powders were confirmed through the SEM images, including the EDS images that exposed the surface terminations of the samples. Topographical studies were carried out using a WiTech Alpha 300 RA atomic force microscope (AFM). Thus, the thickness of the de-sonicated aqueous MXene flakes was quantitatively produced via the tapping mode of the AFM tip. Structure crystallinity and composition were determined using X-Ray Diffraction (XRD) analysis. The quantitative X-ray intensities were captured using a PAN analytical X'Pert PRO powder diffractometer.

2.5 Results and Discussions

The SEM images in **Figure 5** confirmed the fine powder morphology of the synthesized MAX phase. MAX phases are highly dense materials with tightly packed layers, which can be seen from the stacking and cross-sectional views in **Figures 5(b_1-b_2)**. Furthermore, the MAX crystal obtained in **Figure 5a_1** is highly dependent on the elemental precursor materials and heating rates employed during its synthesis.[93] The EDS images in **Figures 5(a_2-a_6)** exhibited the chemical composition of elements (e.g., Ti, and C) expected from these powders. Ti, Al, and C are direct results of the elemental powders, while the presence of O suggests that a slight oxidation of the powders may have occurred during mechanical alloying (MA).[94]

The wide-angle X-ray diffraction is an essential technique and one that validated the successful synthesis of both the MAX phase and MXene specimens. The distinct peaks and valleys of the diffraction pattern validated the crystalline structures of both the MAX phase and MXenes. These intensities were labeled by cross-referencing with established patterns in literature.[95] As can be seen in **Figure 5**, there are ~ ten 312 MAX crystal peaks. These occurred at 2θ = 9.00° (002), 18.59° (004), 33.52° (101), 36.52° (103), 38.30° (104), 41.26° (105), 47.97° (107), 55.91° (109), 55.96° (110), 64.91° (1011). The appearance of these peaks was consistent with the literature albeit with small shifts in the horizontal.[95] The successful etching of MXene was confirmed with the disappearance of all related Ti_3AlC_2 MAX phase peaks and the distinct changes to the (002)/(004) peaks.[95]

There was a general reduction in the intensities of both peaks and the shift of the 004 peaks from 2θ = 18.63° to 12.95° as can be seen in **Figure 5**. The broadening of the 002 peak is also further confirmation of successful Al removal.[95] The presence of other peaks outside the first two is not typical of all MXenes. These peaks starting from 2θ = 34.03° (104) to 65.60° (214) are related to TiC and Al_2O_3 and established contaminants of multilayered MXene structures. [95] Delaminated MXene flakes on the other hand exhibit only the 002 peak usually free of contaminants (e.g., non-etched MAX phases). [54,96]

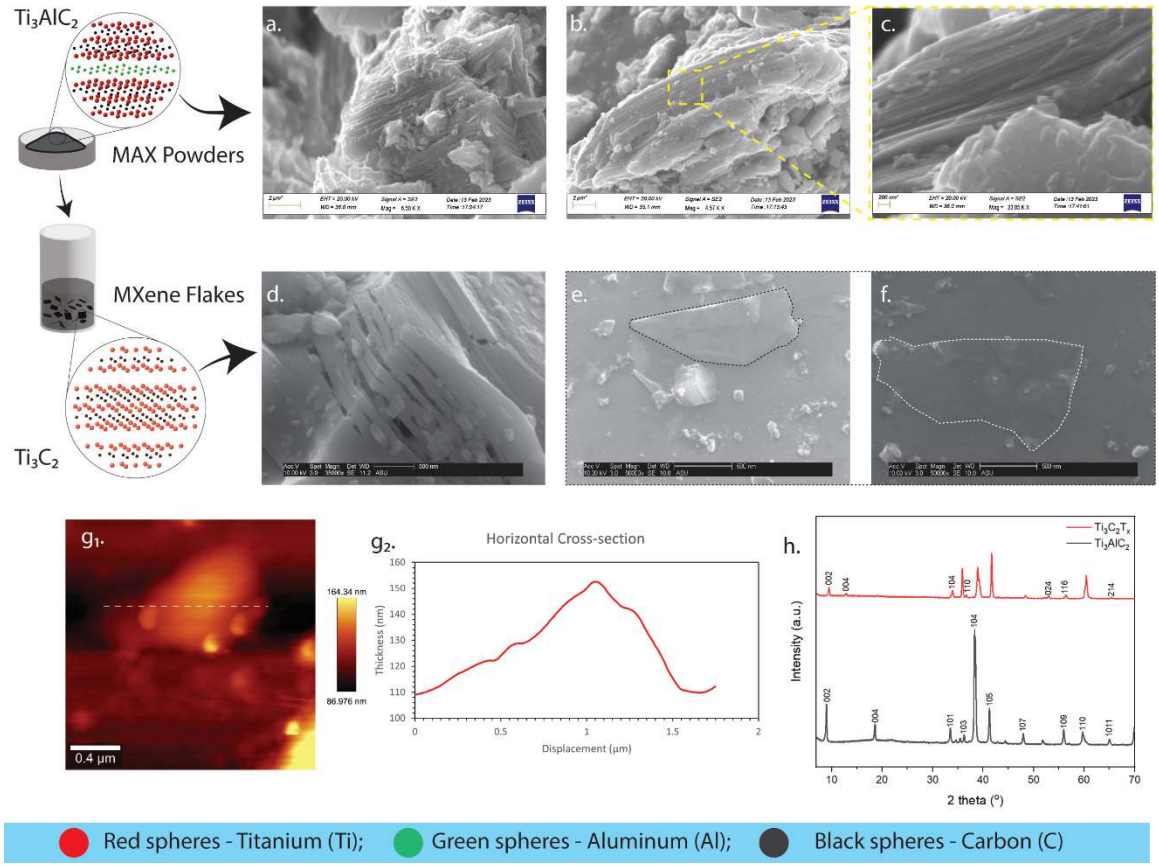

Figure 5. Characterizations of MAX phase and MXene throughout the synthesis process. a.) Frontal SEM micrograph of MAX phase showcasing uniform surface morphology and kink bands, b – c.) Cross-sectional SEM imaging of Ti_3AlC_2 at different resolutions and magnifications, d.) Cross-sectional SEM imaging of multi-layered $Ti_3C_2T_x$ illustrating capacious spacing between layers after etching, e – f.) Delaminated $Ti_3C_2T_x$ sheets at different resolutions, g_1 – g_2.) AFM images depicting cross-sectional thickness of multi-layered $Ti_3C_2T_x$ stack along the horizontal plane, h.) WAXD diffraction patterns of Ti_3AlC_2 before and after etching displaying intensities of MAX phase and resulting MXene at respective phase angles.[92]

CHAPTER 3

DEMONSTRATIONS OF MXENE APPLICATIONS

3.1 Materials

Feedstock for the printing was prepared by dispersing MXene nanoparticles in deionized (DI) water to form aqueous solutions of different concentrations. Isopropyl alcohol/methylbenzene (IPA/toluene) was employed in a 2.25:1 ratio to form 50 mL of antisolvent solution. 0.5 mL of aqueous MXene dispersions (30, 50, 100, and 200 mg mL $^{-1}$) is subsequently added to 1.5 mL IPA/toluene solution. The suspension was then centrifuged at 7800 rpm for 10 min and then vacuum dried at standard room temperature (T ~ 20 ºC). Ensuing desiccation of the samples, the slurries were then re-dispersed in DI water and sonicated for 8 h to create viscous MXene ink. The feedstock was then loaded into a polypropylene fluid dispensing syringe barrel (10-cc, AHS, USA). Finally, the ink was extruded using a motorized fluid dispensing pump system (KD Scientific LEGATO 200). The pulse rate was set at a constant of 0.075 mL min^{-1} and extrusion was carried out for ~ 0.25 min per sample.

3.2 Characterizations

The study of the rheological behavior of MXene dispersions played a crucial role in fine-tuning the printability of the ink. The suitability of the printable inks was ascertained after analysis of viscoelastic parameters (i.e., viscosity, storage modulus, loss modulus). Flow and frequency sweep experiments were carried out on a Discovery HR-2 hybrid rheometer (TA Instruments, DE) with an 8 mm parallel plate, ETC Aluminum system (gap = 50 μm, amount ~ 0.25 mL). All viscoelastic parameters were analyzed in the same shear

rate range (i.e., 0.1 – 100 s^{-1}). The syringe was then attached to an open-source 3D printing system (System 30M, Hyrel, USA). With the setup established, the printing was executed by running the designed G-codes. The printing was carried out on a PVA-coated glass slide (75 * 26 mm). Furthermore, the electrochemical properties of the fabricated MXene ($Ti_3C_2T_x$) were investigated using a three-electrode cell system. $Ti_3C_2T_x$ was allocated the role of the working electrode, Saturated Calomel Electrode (SCE) was employed as the counter electrode, and a platinum wire was utilized as the reference electrode.[97] Aqueous alkaline 1 M KOH solution was the electrolyte used in the electrochemical tests. The CV measurements were obtained using a Parstat 2273 electrochemical system that ran at several scan rates (i.e., 10, 25, 75, and 100 mV s^{-1}) in a constant potential window (-1 to 1 V).

3.3 Results and Discussions

To achieve stable dispersion quality and nanoparticle homogeneity, $Ti_3C_2T_x$ nanoparticles were suspended in aqueous solutions to form different suspension concentrations (i.e., 30, 50, 100, 200 mg mL^{-1} $Ti_3C_2T_x$ content). Furthermore, **Figure 6a** also shows us that all samples tested experience pseudoplastic (non-Newtonian flow) behavior also characterized as shear thinning (i.e., decreasing viscosity with increasing shear rates). The plots highlight the trend and confirm the relatively low viscosities of the lower $Ti_3C_2T_x$ concentrations (i.e., 30, 50 mg mL^{-1}). Consequently, the ink solutions with higher concentrations of $Ti_3C_2T_x$ (i.e., 100, 200 mg mL^{-1}) were utilized for the direct-ink writing (DIW).

More rheological properties were analyzed to draw more concrete conclusions about the aqueous ink solutions. The storage and loss moduli were studied as functions of the oscillation angular frequency, ω, and these results were plotted in **Figures 6(b-c)**. The storage modulus data were used to determine the amount of energy stored in the elastic structure of the material while the loss modulus data provides information about the amount of energy dissipated from the sample. These two parameters when combined provide useful information about the viscoelasticity of the sample. From **Figures 6(b-c)**, the parameters were stable (i.e., little to no fluctuations) for the angular frequency range investigated (i.e., 10^{-1} – 10^{2} rad s^{-1}). Consequently, this makes the ink solutions adequate candidates for deposition on coated substrates and the creation of free-standing architectures.

The storage and loss modulus values were used to help predict the behavior of the fluid after deposition. Furthermore, the viscoelastic models allowed me to predict the complete transition of the ink solution from elastic to viscous behavior. This change occurred at the critical junction ($G' = G''$) Suitable inks delay this transition as long as possible and are consequently a big factor when selecting the inks used to print the patterns in **Figures 6(d-e)**. Consequently, the main trend observed from **Figures 6(a-c)** was that the viscoelastic parameters grew more favorable as a greater concentration of $Ti_3C_2T_x$ was added to the aqueous solution. On the other hand, a balancing act was required to prevent over-densification of the ink which could potentially result in clogging of the printing nozzle.

After the rheology was complete, the 100 and 200 mg mL^{-1} aqueous MXene ink solutions were utilized to create both rectilinear and zig-zag patterns in **Figures 6(d-e)**.

The optical images illustrate the improved deposition and uniformity of the high-$Ti_3C_2T_x$ concentration inks as compared to the low-$Ti_3C_2T_x$ concentration ink solutions observed in previous formulations. The electrical properties of deposits on different substrates were then investigated. Circular dots (diameter ≈ 9.15 mm) of all four concentrations (i.e., 30, 50, 100, 200 mg mL^{-1}) were dropped on a rough substrate. The resistances of the depositions were collected using the two-point probe technique (KEITHLEY multimeter) and the conductivity values were subsequently measured using the following equation.

$\sigma = L/RA$ (14)

where L represents the length of the sample (m), R stands for the resistance measured (**Ω**), A is the cross-sectional area of the sample (m^2), and σ is the conductivity. It can be deduced from **Figure 6f** that the conductivity of the depositions is directly proportional to the $Ti_3C_2T_x$ concentration in the solution. Furthermore, the electrochemical properties of the synthesized samples were then observed using a cyclic voltammetric (CV) study. Different scan rates (i.e., 10, 25, 75, and 100 mv s^{-1}) and as can be seen from **Figures 6(g_1-g_2)** the integral area is directly proportional to the scan rates. This paradigm shift indicates a change in potential as the scan rate increases.[98] The specific capacitance (C_{sp}) of the $Ti_3C_2T_x$-coated electrode was then calculated from the CV curves using the following equation.[99]

$C_{sp} = \int(IdV)/vm\Delta V$ (15)

where C_{sp} is the specific capacitance (F g^{-1}), I represents the current (A), $\int(IdV)$ denotes the integral area under the CV curve, v is the scan rate, m is the mass on the electrode of the system, and ΔV is the change in voltage.

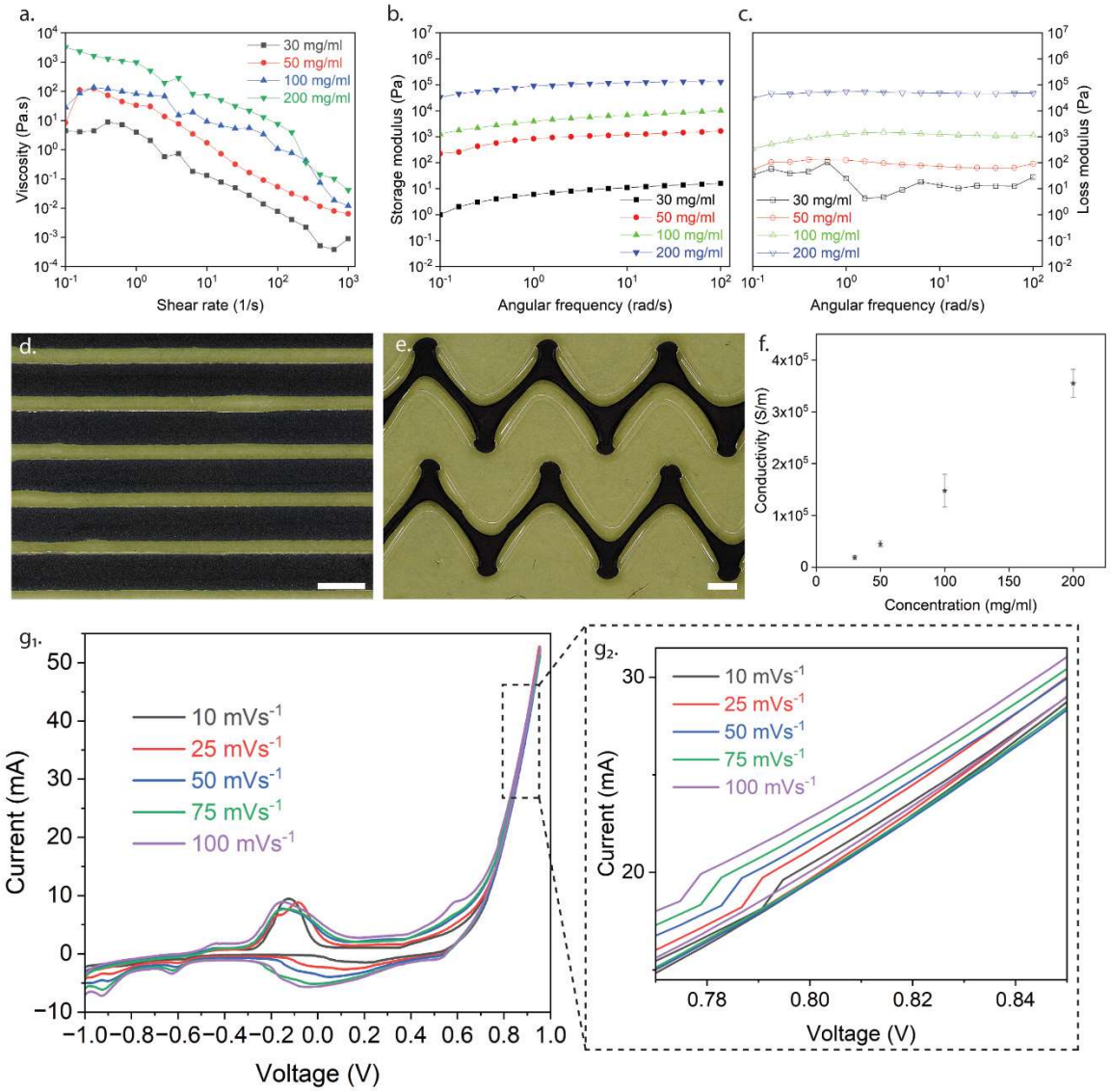

Figure 6. a – c.) Viscoelastic properties of 30, 50, 100, and 200 mg mL^{-1} aqueous $Ti_3C_2T_x$ ink solutions, d – e.) Printed rectilinear and zig-zag patterns of 100 mg mL^{-1} $Ti_3C_2T_x$ ink, f.) Conductivity vs concentration chart for aqueous ink solutions, g_1 – g_2.) CV graph highlighting electrochemical properties of $Ti_3C_2T_x$ – coated electrode at multiple scan speeds.[92]

CHAPTER 4

CONCLUSIONS

This project detailed the synthesis of MXenes from the initial stages to their final deposition forms. Characterizations were then done to analyze their surface morphology, topological features, and their crystal structures via methods of SEM, XRD, AFM, and EDS. Subsequently, these 2D MXene nanoparticles were prepared in polymer inks for 3D printed patterning applications with optimized rheology and printing parameters. This was followed by optical imaging for high-resolution images of the printed patterns.

We have demonstrated the in-house synthesis of MXene and shown its application in 3D-printed patterns and the creation of free-standing architectures. Furthermore, MXenes are highly versatile nanomaterials with massive potential in several industries ranging from wearables due to their flexibility to electromagnetic shield interference in devices. Future work beyond the scope of this project will focus on overcoming issues such as tuning surface functionalities, increasing micropatterning resolutions, and improving the yield of synthesis processes. Finally, we were able to showcase excellent electrical and electrochemical properties which if utilized properly would unlock the vast potential of this modern family and become a valuable asset in the new age.

REFERENCES

(1) Gogotsi, Y.; Anasori, B. The Rise of MXenes. *ACS Nano*. American Chemical Society August 27, 2019, pp 8491–8494. https://doi.org/10.1021/acsnano.9b06394.

(2) Hong, W.; Wyatt, B. C.; Nemani, S. K.; Anasori, B. Double Transition-Metal MXenes: Atomistic Design of Two-Dimensional Carbides and Nitrides. *MRS Bull* **2020**, *45* (10), 850–861. https://doi.org/10.1557/mrs.2020.251.

(3) Hu, T.; Mei, X.; Wang, Y.; Weng, X.; Liang, R.; Wei, M. Two-Dimensional Nanomaterials: Fascinating Materials in Biomedical Field. *Sci Bull (Beijing)* **2019**, *64* (22), 1707–1727. https://doi.org/10.1016/j.scib.2019.09.021.

(4) Bhandary, S.; Sanyal, B. Graphene-Boron Nitride Composite: A Material with Advanced Functionalities. In *Composites and Their Properties*; InTech, 2012. https://doi.org/10.5772/50729.

(5) Wu, M.-X.; Yang, Y.-W. Applications of Covalent Organic Frameworks (COFs): From Gas Storage and Separation to Drug Delivery. *Chinese Chemical Letters* **2017**, *28* (6), 1135–1143. https://doi.org/10.1016/j.cclet.2017.03.026.

(6) Nieto, S.; Toro, N.; Robles, P.; Gálvez, E.; Gallegos, S.; Jeldres, R. I. Flocculation of Clay-Based Tailings: Differences of Kaolin and Sodium Montmorillonite in Salt Medium. *Materials* **2022**, *15* (3), 1156. https://doi.org/10.3390/ma15031156.

(7) Gusmão, R.; Sofer, Z.; Pumera, M. Black Phosphorus Rediscovered: From Bulk Material to Monolayers. *Angewandte Chemie International Edition* **2017**, *56* (28), 8052–8072. https://doi.org/10.1002/anie.201610512.

(8) Guo, H.; Barnard, A. S. Naturally Occurring Iron Oxide Nanoparticles: Morphology, Surface Chemistry, and Environmental Stability. *J. Mater. Chem. A* **2013**, *1* (1), 27–42. https://doi.org/10.1039/C2TA00523A.

(9) Naguib, M.; Mochalin, V. N.; Barsoum, M. W.; Gogotsi, Y. 25th Anniversary Article: MXenes: A New Family of Two-Dimensional Materials. *Advanced Materials* **2014**, *26* (7), 992–1005. https://doi.org/10.1002/adma.201304138.

(10) Novoselov, K. S.; Geim, A. K.; Morozov, S. v.; Jiang, D.; Zhang, Y.; Dubonos, S. v.; Grigorieva, I. v.; Firsov, A. A. Electric Field Effect in Atomically Thin Carbon Films. *Science (1979)* **2004**, *306* (5696), 666–669. https://doi.org/10.1126/science.1102896.

(11) Saba, N.; Jawaid, M. Functionalized Graphene Reinforced Hybrid Nanocomposites, and Their Applications. In *Functionalized Graphene Nanocomposites and their Derivatives*; Elsevier, 2019; pp 205–218. https://doi.org/10.1016/B978-0-12-814548-7.00010-6.

(12) Baig, N.; Kammakakam, I.; Falath, W. Nanomaterials: A Review of Synthesis Methods, Properties, Recent Progress, and Challenges. *Mater Adv* **2021**, *2* (6), 1821–1871. https://doi.org/10.1039/D0MA00807A.

(13) Wu, Q.; Miao, W.; Zhang, Y.; Gao, H.; Hui, D. Mechanical Properties of Nanomaterials: A Review. *Nanotechnol Rev* **2020**, *9* (1), 259–273. https://doi.org/10.1515/ntrev-2020-0021.

(14) Saleh, T. A. Nanomaterials: Classification, Properties, and Environmental Toxicities. *Environ Technol Innov* **2020**, *20*, 101067. https://doi.org/10.1016/j.eti.2020.101067.

(15) Rizwan, M.; Shoukat, A.; Ayub, A.; Razzaq, B.; Tahir, M. B. Types and Classification of Nanomaterials. In *Nanomaterials: Synthesis, Characterization, Hazards, and Safety*; Elsevier, 2021; pp 31–54. https://doi.org/10.1016/B978-0-12-823823-3.00001-X.

(16) Sivasankarapillai, V. S.; Somakumar, A. K.; Joseph, J.; Nikazar, S.; Rahdar, A.; Kyzas, G. Z. Cancer Theranostic Applications of MXene Nanomaterials: Recent Updates. *Nano-Structures & Nano-Objects* **2020**, *22*, 100457. https://doi.org/10.1016/j.nanoso.2020.100457.

(17) Zahmatkesh, S.; Hajiaghaei-Keshteli, M.; Bokhari, A.; Sundaramurthy, S.; Panneerselvam, B.; Rezakhani, Y. Wastewater Treatment with Nanomaterials for the Future: A State-of-the-Art Review. *Environ Res* **2022**, 114652. https://doi.org/10.1016/j.envres.2022.114652.

(18) Simón-Vázquez, R.; Peleteiro, M.; Lozano, T.; González-Fernández, Á.; Casal, A. Nanotoxicology; 2012; pp 443–485. https://doi.org/10.1016/B978-0-12-415769-9.00015-7.

(19) Rafique, M.; Tahir, M. B.; Rafique, M. S.; Safdar, N.; Tahir, R. Nanostructure Materials and Their Classification by Dimensionality. In *Nanotechnology and Photocatalysis for Environmental Applications*; Elsevier, 2020; pp 27–44. https://doi.org/10.1016/B978-0-12-821192-2.00002-4.

(20) Chethan, B.; Megha, R.; Vijayakumari, S. C.; Ravikiran, Y. T.; Prakash, H. G. R.; Thomas, S. Nanostructures for Humidity Sensing and Photocatalytic Applications. In *Nanoscale Processing*; Elsevier, 2021; pp 327–359. https://doi.org/10.1016/B978-0-12-820569-3.00012-8.

(21) Razali, M. H.; Ismail, N. A. Basic Concepts and Processing of Nanostructures Materials. In *Nanoscale Processing*; Elsevier, 2021; pp 1–32. https://doi.org/10.1016/B978-0-12-820569-3.00001-3.

(22) Ilangovan, R.; Subha, V.; Ravindran, R. S. E.; Kirubanandan, S.; Renganathan, S. Nanomaterials: Synthesis, Physicochemical Characterization, and Biopharmaceutical Applications. In *Nanoscale Processing*; Elsevier, 2021; pp 33–70. https://doi.org/10.1016/B978-0-12-820569-3.00002-5.

(23) Karaca, B.; Karataş, Y.; Cakar, A. B.; Gülcan, M.; Şen, F. Carbon-Based Nanostructures, and Nanomaterials. In *Nanoscale Processing*; Elsevier, 2021; pp 103–130. https://doi.org/10.1016/B978-0-12-820569-3.00004-9.

(24) Feng, H.; Tang, L.; Zeng, G.; Zhou, Y.; Deng, Y.; Ren, X.; Song, B.; Liang, C.; Wei, M.; Yu, J. Core-Shell Nanomaterials: Applications in Energy Storage and Conversion. *Adv Colloid Interface Sci* **2019**, *267*, 26–46. https://doi.org/10.1016/j.cis.2019.03.001.

(25) Hecht, J. Nanomaterials Pave the Way for the Next Computing Generation. *Nature* **2022**, *608* (7922), S2–S3. https://doi.org/10.1038/d41586-022-02147-3.

(26) Pradhan, K. K.; Chakraverty, S. Introduction to Nanostructures. In *Nano Scaled Structural Problems*; AIP Publishing, 2021; pp 1–10. https://doi.org/10.1063/9780735422865_001.

(27) Kumar, S.; Bhushan, P.; Bhattacharya, S. Fabrication of Nanostructures with Bottom-up Approach and Their Utility in Diagnostics, Therapeutics, and Others; 2018; pp 167–198. https://doi.org/10.1007/978-981-10-7751-7_8.

(28) Holkar, C. R.; Jain, S. S.; Jadhav, A. J.; Pinjari, D. v. Scale-Up Technologies for Advanced Nanomaterials for Green Energy. In *Nanomaterials for Green Energy*; Elsevier, 2018; pp 433–455. https://doi.org/10.1016/B978-0-12-813731-4.00014-X.

(29) Omar, G.; Salim, M. A.; Mizah, B. R.; Kamarolzaman, A. A.; Nadlene, R. Electronic Applications of Functionalized Graphene Nanocomposites. In *Functionalized Graphene Nanocomposites and their Derivatives*; Elsevier, 2019; pp 245–263. https://doi.org/10.1016/B978-0-12-814548-7.00012-X.

(30) Verma, D.; Goh, K. L. Functionalized Graphene-Based Nanocomposites for Energy Applications. In *Functionalized Graphene Nanocomposites and their Derivatives*; Elsevier, 2019; pp 219–243. https://doi.org/10.1016/B978-0-12-814548-7.00011-8.

(31) Dolez, P. I. Nanomaterials Definitions, Classifications, and Applications. In *Nanoengineering*; Elsevier, 2015; pp 3–40. https://doi.org/10.1016/B978-0-444-62747-6.00001-4.

(32) Buzea, C.; Pacheco, I. Nanomaterials and Their Classification; 2017; pp 3–45. https://doi.org/10.1007/978-81-322-3655-9_1.

(33) Sannino, D. Types and Classification of Nanomaterials. In *Nanotechnology*; Springer Singapore: Singapore, 2021; pp 15–38. https://doi.org/10.1007/978-981-15-9437-3_2.

(34) Stone, V.; Nowack, B.; Baun, A.; van den Brink, N.; von der Kammer, F.; Dusinska, M.; Handy, R.; Hankin, S.; Hassellöv, M.; Joner, E.; Fernandes, T. F. Nanomaterials for Environmental Studies: Classification, Reference Material Issues, and Strategies for Physico-Chemical Characterisation. *Science of The Total Environment* **2010**, *408* (7), 1745–1754. https://doi.org/10.1016/j.scitotenv.2009.10.035.

(35) Sudha, P. N.; Sangeetha, K.; Vijayalakshmi, K.; Barhoum, A. Nanomaterials History, Classification, Unique Properties, Production, and Market. In *Emerging Applications of Nanoparticles and Architecture Nanostructures*; Elsevier, 2018; pp 341–384. https://doi.org/10.1016/B978-0-323-51254-1.00012-9.

(36) Khan, F. A. Nanomaterials: Types, Classifications, and Sources. In *Applications of Nanomaterials in Human Health*; Springer Singapore: Singapore, 2020; pp 1–13. https://doi.org/10.1007/978-981-15-4802-4_1.

(37) Glezer, A. M. Structural Classification of Nanomaterials. *Russian Metallurgy (Metally)* **2011**, *2011* (4), 263–269. https://doi.org/10.1134/S0036029511040057.

(38) Huang, R.; Luther, D. C.; Zhang, X.; Gupta, A.; Tufts, S. A.; Rotello, V. M. Engineering the Interface between Inorganic Nanoparticles and Biological Systems through Ligand Design. *Nanomaterials* **2021**, *11* (4), 1001. https://doi.org/10.3390/nano11041001.

(39) Taghipour, S.; Hosseini, S. M.; Ataie-Ashtiani, B. Engineering Nanomaterials for Water and Wastewater Treatment: Review of Classifications, Properties and Applications. *New Journal of Chemistry* **2019**, *43* (21), 7902–7927. https://doi.org/10.1039/C9NJ00157C.

(40) Hu, M.; Zhang, H.; Hu, T.; Fan, B.; Wang, X.; Li, Z. Emerging 2D MXenes for Supercapacitors: Status, Challenges and Prospects. *Chem Soc Rev* **2020**, *49* (18), 6666–6693. https://doi.org/10.1039/D0CS00175A.

(41) Liu, F.; Zhou, A.; Chen, J.; Jia, J.; Zhou, W.; Wang, L.; Hu, Q. Preparation of Ti_3C_2 and Ti_2C MXenes by Fluoride Salts Etching and Methane Adsorptive Properties. *Appl Surf Sci* **2017**, *416*, 781–789. https://doi.org/10.1016/j.apsusc.2017.04.239.

(42) Feng, A.; Yu, Y.; Wang, Y.; Jiang, F.; Yu, Y.; Mi, L.; Song, L. Two-Dimensional MXene Ti_3C_2 Produced by Exfoliation of Ti_3AlC_2. *Mater Des* **2017**, *114*, 161–166. https://doi.org/10.1016/j.matdes.2016.10.053.

(43) Zhang, H. Ultrathin Two-Dimensional Nanomaterials. *ACS Nano* **2015**, *9* (10), 9451–9469. https://doi.org/10.1021/acsnano.5b05040.

(44) Zhang, T.; Pan, L.; Tang, H.; Du, F.; Guo, Y.; Qiu, T.; Yang, J. Synthesis of Two-Dimensional $Ti_3C_2T_x$ MXene Using HCl+LiF Etchant: Enhanced Exfoliation and Delamination. *J Alloys Compd* **2017**, *695*, 818–826. https://doi.org/10.1016/j.jallcom.2016.10.127.

(45) Guidelines for Synthesis and Processing of Two-Dimensional Titanium Carbide ($Ti_3C_2T_x$ MXene).

(46) Zhang, C. J.; Pinilla, S.; McEvoy, N.; Cullen, C. P.; Anasori, B.; Long, E.; Park, S. H.; Seral-Ascaso, A.; Shmeliov, A.; Krishnan, D.; Morant, C.; Liu, X.; Duesberg, G. S.; Gogotsi, Y.; Nicolosi, V. Oxidation Stability of Colloidal Two-Dimensional Titanium Carbides (MXenes). *Chemistry of Materials* **2017**, *29* (11), 4848–4856. https://doi.org/10.1021/acs.chemmater.7b00745.

(47) Lipatov, A.; Lu, H.; Alhabeb, M.; Anasori, B.; Gruverman, A.; Gogotsi, Y.; Sinitskii, A. *Elastic Properties of 2D $Ti_3C_2T_x$ MXene Monolayers and Bilayers*; 2018. https://www.science.org.

(48) Li, G.; Tan, L.; Zhang, Y.; Wu, B.; Li, L. Highly Efficiently Delaminated Single-Layered MXene Nanosheets with Large Lateral Size. *Langmuir* **2017**, *33* (36), 9000–9006. https://doi.org/10.1021/acs.langmuir.7b01339.

(49) Wang, X.; Garnero, C.; Rochard, G.; Magne, D.; Morisset, S.; Hurand, S.; Chartier, P.; Rousseau, J.; Cabioc'h, T.; Coutanceau, C.; Mauchamp, V.; Célérier, S. A New Etching Environment (FeF_3/HCl) for the Synthesis of Two-Dimensional Titanium Carbide MXenes: A Route towards Selective Reactivity vs. Water. *J. Mater. Chem. A* **2017**, *5* (41), 22012–22023. https://doi.org/10.1039/C7TA01082F.

(50) Alhabeb, M.; Maleski, K.; Mathis, T. S.; Sarycheva, A.; Hatter, C. B.; Uzun, S.; Levitt, A.; Gogotsi, Y. Selective Etching of Silicon from Ti_3SiC_2 (MAX) To Obtain 2D Titanium Carbide (MXene). *Angewandte Chemie International Edition* **2018**, *57* (19), 5444–5448. https://doi.org/10.1002/anie.201802232.

(51) Lipatov, A.; Lu, H.; Alhabeb, M.; Anasori, B.; Gruverman, A.; Gogotsi, Y.; Sinitskii, A. *Elastic Properties of 2D $Ti_3C_2T_x$ MXene Monolayers and Bilayers*; 2018. https://www.science.org.

(52) Anasori, B.; Xie, Y.; Beidaghi, M.; Lu, J.; Hosler, B. C.; Hultman, L.; Kent, P. R. C.; Gogotsi, Y.; Barsoum, M. W. Two-Dimensional, Ordered, Double Transition Metals Carbides (MXenes). *ACS Nano* **2015**, *9* (10), 9507–9516. https://doi.org/10.1021/acsnano.5b03591.

(53) Zhang, T.; Pan, L.; Tang, H.; Du, F.; Guo, Y.; Qiu, T.; Yang, J. Synthesis of Two-Dimensional $Ti_3C_2T_x$ MXene Using HCl+LiF Etchant: Enhanced Exfoliation and Delamination. *J Alloys Compd* **2017**, *695*, 818–826. https://doi.org/10.1016/j.jallcom.2016.10.127.

(54) Jambhulkar, S.; Liu, S.; Vala, P.; Xu, W.; Ravichandran, D.; Zhu, Y.; Bi, K.; Nian, Q.; Chen, X.; Song, K. Aligned $Ti_3C_2T_x$ MXene for 3D Micropatterning via Additive Manufacturing. *ACS Nano* **2021**, *15* (7), 12057–12068. https://doi.org/10.1021/acsnano.1c03388.

(55) Husmann, S.; Budak, Ö.; Shim, H.; Liang, K.; Aslan, M.; Kruth, A.; Quade, A.; Naguib, M.; Presser, V. *Ionic Liquid-Based Synthesis of MXene*; 2020.

(56) Shi, H.; Zhang, P.; Liu, Z.; Park, S. W.; Lohe, M. R.; Wu, Y.; Shaygan Nia, A.; Yang, S.; Feng, X. Ambient-Stable Two-Dimensional Titanium Carbide (MXene) Enabled by Iodine Etching. *Angewandte Chemie - International Edition* **2021**, *60* (16), 8689–8693. https://doi.org/10.1002/anie.202015627.

(57) Naguib, M.; Kurtoglu, M.; Presser, V.; Lu, J.; Niu, J.; Heon, M.; Hultman, L.; Gogotsi, Y.; Barsoum, M. W. Two-Dimensional Nanocrystals Produced by Exfoliation of Ti_3AlC_2. *Advanced Materials* **2011**, *23* (37), 4248–4253. https://doi.org/10.1002/adma.201102306.

(58) Xiong, D.; Li, X.; Bai, Z.; Lu, S. Recent Advances in Layered $Ti_3C_2T_x$ MXene for Electrochemical Energy Storage. *Small* **2018**, *14* (17), 1703419. https://doi.org/10.1002/smll.201703419.

(59) Alhabeb, M.; Maleski, K.; Mathis, T. S.; Sarycheva, A.; Hatter, C. B.; Uzun, S.; Levitt, A.; Gogotsi, Y. Selective Etching of Silicon from Ti_3SiC_2 (MAX) To Obtain 2D Titanium Carbide (MXene). *Angewandte Chemie International Edition* **2018**, *57* (19), 5444–5448. https://doi.org/10.1002/anie.201802232.

(60) Halim, J.; Kota, S.; Lukatskaya, M. R.; Naguib, M.; Zhao, M.-Q.; Moon, E. J.; Pitock, J.; Nanda, J.; May, S. J.; Gogotsi, Y.; Barsoum, M. W. Synthesis and Characterization of 2D Molybdenum Carbide (MXene). *Adv Funct Mater* **2016**, *26* (18), 3118–3127. https://doi.org/10.1002/adfm.201505328.

(61) Ghidiu, M.; Naguib, M.; Shi, C.; Mashtalir, O.; Pan, L. M.; Zhang, B.; Yang, J.; Gogotsi, Y.; Billinge, S. J. L.; Barsoum, M. W. Synthesis and Characterization of Two-Dimensional Nb_4C_3 (MXene). *Chem. Commun.* **2014**, *50* (67), 9517–9520. https://doi.org/10.1039/C4CC03366C.

(62) Soundiraraju, B.; George, B. K. Two-Dimensional Titanium Nitride (Ti_2N) MXene: Synthesis, Characterization, and Potential Application as Surface-Enhanced Raman Scattering Substrate. *ACS Nano* **2017**, *11* (9), 8892–8900. https://doi.org/10.1021/acsnano.7b03129.

(63) Deysher, G.; Shuck, C. E.; Hantanasirisakul, K.; Frey, N. C.; Foucher, A. C.; Maleski, K.; Sarycheva, A.; Shenoy, V. B.; Stach, E. A.; Anasori, B.; Gogotsi, Y. Synthesis of MoVAlC MAX Phase and Two-Dimensional MoVC MXene with Five Atomic Layers of Transition Metals. *ACS Nano* **2020**, *14* (1), 204–217. https://doi.org/10.1021/acsnano.9b07708.

(64) Shen, C.; Wang, L.; Zhou, A.; Wang, B.; Wang, X.; Lian, W.; Hu, Q.; Qin, G.; Liu, X. Synthesis and Electrochemical Properties of Two-Dimensional RGO/$Ti_3C_2T_x$ Nanocomposites. *Nanomaterials* **2018**, *8* (2), 80. https://doi.org/10.3390/nano8020080.

(65) Halim, J.; Kota, S.; Lukatskaya, M. R.; Naguib, M.; Zhao, M.-Q.; Moon, E. J.; Pitock, J.; Nanda, J.; May, S. J.; Gogotsi, Y.; Barsoum, M. W. Synthesis and Characterization of 2D Molybdenum Carbide (MXene). *Adv Funct Mater* **2016**, *26* (18), 3118–3127. https://doi.org/10.1002/adfm.201505328.

(66) Naguib, M.; Mashtalir, O.; Carle, J.; Presser, V.; Lu, J.; Hultman, L.; Gogotsi, Y.; Barsoum, M. W. Two-Dimensional Transition Metal Carbides. *ACS Nano* **2012**, *6* (2), 1322–1331. https://doi.org/10.1021/nn204153h.

(67) Athar, T. Smart Precursors for Smart Nanoparticles. In *Emerging Nanotechnologies for Manufacturing*; Elsevier, 2015; pp 444–538. https://doi.org/10.1016/B978-0-323-28990-0.00017-8.

(68) Srivastava, A.; Verma, A.; Prajapati, Y. K. Effect of 2D, TMD, Perovskite, and 2D Transition Metal Carbide/Nitride Materials on Performance Parameters of SPR Biosensor. In *Handbook of Nanomaterials for Sensing Applications*; Elsevier, 2021; pp 57–90. https://doi.org/10.1016/B978-0-12-820783-3.00005-1.

(69) Barsoum, M. W.; El-Raghy, T. Synthesis and Characterization of a Remarkable Ceramic: Ti_3SiC_2. *Journal of the American Ceramic Society* **1996**, *79* (7), 1953–1956. https://doi.org/10.1111/j.1151-2916.1996.tb08018.x.

(70) Lapauw, T.; Swarnakar, A. K.; Tunca, B.; Lambrinou, K.; Vleugels, J. Nanolaminated Ternary Carbide (MAX Phase) Materials for High-Temperature Applications. *Int J Refract Metals Hard Mater* **2018**, *72*, 51–55. https://doi.org/10.1016/j.ijrmhm.2017.11.038.

(71) Wang, X. H.; Zhou, Y. C. Layered Machinable and Electrically Conductive Ti_2AlC and Ti_3AlC_2 Ceramics: A Review. *J Mater Sci Technol* **2010**, *26* (5), 385–416. https://doi.org/10.1016/S1005-0302(10)60064-3.

(72) Muradyan, G. N.; Dolukhanyan, S. .K.; Aleksanyan, A. .G.; Ter-Galstyan, O. .P.; Mnatsakanyan, N. .L.; Asatryan, K. .V.; Mardanyan, S. .S.; Hovhannisyan, A. A. Synthesis in Hydride Cycle of Ti–Al–C Based MAX Phases from Mixtures of Titanium Carbohydrides and Aluminum Powders. *Ceram Int* **2022**. https://doi.org/10.1016/j.ceramint.2022.11.125.

(73) Gauthier-Brunet, V.; Cabioc'h, T.; Chartier, P.; Jaouen, M.; Dubois, S. Reaction Synthesis of Layered Ternary Ti_2AlC Ceramic. *J Eur Ceram Soc* **2009**, *29* (1), 187–194. https://doi.org/10.1016/j.jeurceramsoc.2008.05.039.

(74) Dong, P.; Wang, Z.; Wang, W.; Chen, S.; Zhou, J. Understanding the Spark Plasma Sintering from the View of Materials Joining. *Scr Mater* **2016**, *123*, 118–121. https://doi.org/10.1016/j.scriptamat.2016.06.014.

(75) Santanach, J. G.; Estournès, C.; Weibel, A.; Chevallier, G.; Bley, V.; Laurent, C.; Peigney, A. Influence of Pulse Current during Spark Plasma Sintering Evidenced on Reactive Alumina–Hematite Powders. *J Eur Ceram Soc* **2011**, *31* (13), 2247–2254. https://doi.org/10.1016/j.jeurceramsoc.2011.06.003.

(76) Song, X.; Liu, X.; Zhang, J. Neck Formation and Self-Adjusting Mechanism of Neck Growth of Conducting Powders in Spark Plasma Sintering. *Journal of the American Ceramic Society* **2006**, *89* (2), 494–500. https://doi.org/10.1111/j.1551-2916.2005.00777.x.

(77) Zhang, Z.; Wang, L.; Wang, J.; Jiang, X.; Li, X.; Hu, Z.; Ji, Y.; Wu, X.; Chen, C. Mesoporous Silica-Coated Gold Nanorods as a Light-Mediated Multifunctional Theranostic Platform for Cancer Treatment. *Advanced Materials* **2012**, *24* (11), 1418–1423. https://doi.org/10.1002/adma.201104714.

(78) Orrù, R.; Cao, G. Ultra-High Temperature Ceramics by Spark Plasma Sintering. In *Spark Plasma Sintering*; Elsevier, 2019; pp 49–76. https://doi.org/10.1016/B978-0-12-817744-0.00002-7.

(79) Licheri, R.; Orrù, R.; Musa, C.; Cao, G. Combination of SHS and SPS Techniques for Fabrication of Fully Dense ZrB_2-ZrC-SiC Composites. *Mater Lett* **2008**, *62* (3), 432–435. https://doi.org/10.1016/j.matlet.2007.05.066.

(80) Varma, A.; Rogachev, A. S.; Mukasyan, A. S.; Hwang, S. Combustion Synthesis of Advanced Materials: Principles and Applications; 1998; pp 79–226. https://doi.org/10.1016/S0065-2377(08)60093-9.

(81) Verger, L.; Xu, C.; Natu, V.; Cheng, H.-M.; Ren, W.; Barsoum, M. W. Overview of the Synthesis of MXenes and Other Ultrathin 2D Transition Metal Carbides and Nitrides. *Curr Opin Solid State Mater Sci* **2019**, *23* (3), 149–163. https://doi.org/10.1016/j.cossms.2019.02.001.

(82) Ossila.com. *2D Materials: An Introduction to Two-Dimensional Materials*.

(83) Wei, Y.; Zhang, P.; Soomro, R. A.; Zhu, Q.; Xu, B. Advances in the Synthesis of 2D MXenes. *Advanced Materials* **2021**, *33* (39), 2103148. https://doi.org/10.1002/adma.202103148.

(84) Ghidiu, M.; Lukatskaya, M. R.; Zhao, M.-Q.; Gogotsi, Y.; Barsoum, M. W. Conductive Two-Dimensional Titanium Carbide 'Clay' with High Volumetric Capacitance. *Nature* **2014**, *516* (7529), 78–81. https://doi.org/10.1038/nature13970.

(85) Halim, J.; Lukatskaya, M. R.; Cook, K. M.; Lu, J.; Smith, C. R.; Näslund, L.-Å.; May, S. J.; Hultman, L.; Gogotsi, Y.; Eklund, P.; Barsoum, M. W. Transparent Conductive Two-Dimensional Titanium Carbide Epitaxial Thin Films. *Chemistry of Materials* **2014**, *26* (7), 2374–2381. https://doi.org/10.1021/cm500641a.

(86) Wu, J.; Wang, Y.; Zhang, Y.; Meng, H.; Xu, Y.; Han, Y.; Wang, Z.; Dong, Y.; Zhang, X. Highly Safe and Ionothermal Synthesis of Ti3C2 MXene with Expanded Interlayer Spacing for Enhanced Lithium Storage. *Journal of Energy Chemistry* **2020**, *47*, 203–209. https://doi.org/10.1016/j.jechem.2019.11.029.

(87) Li, T.; Yao, L.; Liu, Q.; Gu, J.; Luo, R.; Li, J.; Yan, X.; Wang, W.; Liu, P.; Chen, B.; Zhang, W.; Abbas, W.; Naz, R.; Zhang, D. Fluorine-Free Synthesis of High-Purity $Ti_3C_2T_x$ (T=OH, O) via Alkali Treatment. *Angewandte Chemie International Edition* **2018**, *57* (21), 6115–6119. https://doi.org/10.1002/anie.201800887.

(88) Chen, J.; Jin, Q.; Li, Y.; Shao, H.; Liu, P.; Liu, Y.; Taberna, P.; Huang, Q.; Lin, Z.; Simon, P. Molten Salt-Shielded Synthesis (MS^3) of MXenes in Air. *ENERGY & ENVIRONMENTAL MATERIALS* **2022**. https://doi.org/10.1002/eem2.12328.

(89) Sang, X.; Xie, Y.; Lin, M.-W.; Alhabeb, M.; van Aken, K. L.; Gogotsi, Y.; Kent, P. R. C.; Xiao, K.; Unocic, R. R. Atomic Defects in Monolayer

Titanium Carbide ($Ti_3C_2T_x$) MXene. *ACS Nano* **2016**, *10* (10), 9193–9200. https://doi.org/10.1021/acsnano.6b05240.

(90) Zhou, J.; Zha, X.; Zhou, X.; Chen, F.; Gao, G.; Wang, S.; Shen, C.; Chen, T.; Zhi, C.; Eklund, P.; Du, S.; Xue, J.; Shi, W.; Chai, Z.; Huang, Q. Synthesis and Electrochemical Properties of Two-Dimensional Hafnium Carbide. *ACS Nano* **2017**, *11* (4), 3841–3850. https://doi.org/10.1021/acsnano.7b00030.

(91) Zhou, J.; Zha, X.; Chen, F. Y.; Ye, Q.; Eklund, P.; Du, S.; Huang, Q. A Two-Dimensional Zirconium Carbide by Selective Etching of Al_3C_3 from Nanolaminated $Zr_3Al_3C_5$. *Angewandte Chemie International Edition* **2016**, *55* (16), 5008–5013. https://doi.org/10.1002/anie.201510432.

(92) Fagade, M.; Patil, D.; Thummalapalli, S. V.; Jambhulkar, S.; Ravichandran, D.; Kannan Arunachala M.; Song, K. 3D Printing Aqueous $Ti_3C_2T_x$ Inks for MXene-Based Energy Devices. *The Royal Society of Chemistry* **2023**.

(93) Shuck, C. E.; Han, M.; Maleski, K.; Hantanasirisakul, K.; Kim, S. J.; Choi, J.; Reil, W. E. B.; Gogotsi, Y. Effect of Ti_3AlC_2 MAX Phase on Structure and Properties of Resultant $Ti_3C_2T_x$ MXene. *ACS Appl Nano Mater* **2019**, *2* (6), 3368–3376. https://doi.org/10.1021/acsanm.9b00286.

(94) Von Treifeldt, J. E.; Firestein, K. L.; Fernando, J. F. S.; Zhang, C.; Siriwardena, D. P.; Lewis, C.-E. M.; Golberg, D. v. The Effect of Ti_3AlC_2 MAX Phase Synthetic History on the Structure and Electrochemical Properties of Resultant Ti_3C_2 MXenes. *Mater Des* **2021**, *199*, 109403. https://doi.org/10.1016/j.matdes.2020.109403.

(95) Scheibe, B.; Kupka, V.; Peplińska, B.; Jarek, M.; Tadyszak, K. The Influence of Oxygen Concentration during MAX Phases (Ti_3AlC_2) Preparation on the α-Al_2O_3 Microparticles Content and Specific Surface Area of Multilayered MXenes ($Ti_3C_2T_x$). *Materials* **2019**, *12* (3), 353. https://doi.org/10.3390/ma12030353.

(96) Biswas, S.; Alegaonkar, P. S. MXene: Evolutions in Chemical Synthesis and Recent Advances in Applications. *Surfaces* **2021**, *5* (1), 1–36. https://doi.org/10.3390/surfaces5010001.

(97) Zhang, Y.; Zhao, Z.; Luo, C.; Wu, X.; Chen, W. Toward Understanding the Electrochemical Capacitance Mechanism of MXene by Intercalation of Inorganic Ions and Organic Macromolecular Ions. *Appl Surf Sci* **2022**, *578*, 152030. https://doi.org/10.1016/j.apsusc.2021.152030.

(98) Lukatskaya, M. R.; Kota, S.; Lin, Z.; Zhao, M.-Q.; Shpigel, N.; Levi, M. D.; Halim, J.; Taberna, P.-L.; Barsoum, M. W.; Simon, P.; Gogotsi, Y. Ultra-High-Rate Pseudocapacitive Energy Storage in Two-Dimensional Transition

Metal Carbides. *Nat Energy* **2017**, *2* (8), 17105. https://doi.org/10.1038/nenergy.2017.105.

(99) Jiang, Q.; Lei, Y.; Liang, H.; Xi, K.; Xia, C.; Alshareef, H. N. Review of MXene Electrochemical Microsupercapacitors. *Energy Storage Mater* **2020**, *27*, 78–95. https://doi.org/10.1016/j.ensm.2020.01.018.